# 9

#### Research article

Véronique Many, Romain Dézert, Etienne Duguet, Alexandre Baron, Vikas Jangid, Virginie Ponsinet, Serge Ravaine, Philippe Richetti, Philippe Barois and Mona Tréguer-Delapierre\*

# High optical magnetism of dodecahedral plasmonic meta-atoms

https://doi.org/10.1515/nanoph-2018-0175 Received October 17, 2018; revised November 24, 2018; accepted December 3, 2018

**Abstract:** The generation in artificial composites of a magnetic response to light, comparable in magnitude with the natural electric response, may offer an invaluable control parameter for a fine steering of light at the nanoscale. In many experimental realizations, however, the magnetic response of artificial meta-atoms is too weak so that there is a need for new designs with increased magnetic polarizability. Numerical simulations show that geometrical plasmonic nanostructures based on Platonic solids are excellent candidates for the production of strong optical magnetism in visible light. Inspired by these models, we report a bottom-up approach to synthesize plasmonic nanoclusters made of 12 gold patches located at the center of the faces of a dodecahedron. The scattering of the electric and magnetic dipole induced by light is measured across the whole visible range. The ratio of the magnetic to electric response at resonance is found three times higher than its counterpart measured on disordered plasmonic clusters ("plasmonic raspberries") of the same size. Numerical simulations confirm the experimental measurements of the magnetic response.

**Keywords:** gold dodecapods; meta-atoms; optical magnetism; plasmonic raspberries; plasmonics.

https://orcid.org/0000-0002-3096-6645

**Véronique Many:** Université de Bordeaux, CNRS, ICMCB, UMR 5026, Pessac 33600, France; and Université de Bordeaux, CNRS, CRPP, UMR 5031, Pessac 33600, France

Romain Dézert, Alexandre Baron, Vikas Jangid, Virginie Ponsinet, Serge Ravaine, Philippe Richetti and Philippe Barois: Université de Bordeaux, CNRS, CRPP, UMR 5031, Pessac 33600, France Etienne Duguet: Université de Bordeaux, CNRS, ICMCB, UMR 5026, Pessac 33600, France

## 1 Introduction

The search for artificial optical magnetism in engineered composites has attracted intense research efforts since the emergence of the concept of metamaterials in 2000 [1]. Although the optical properties of conventional materials or systems are governed by the sole electric polarizability, controlling the magnetic polarizability would offer an additional lever, potentially enabling a full control of the amplitude and the phase of a light wave transmitted through and reflected from an interface. Many applications of bulk materials or optical films made of magneto-electric elements exhibiting optical magnetism have been proposed by theories such as total transmission or reflection (Huyghens' surfaces), band-pass filtering, pulse compression, directional steering of light, polarization beam splitters, converters, and analyzers, to name a few [2]. In natural materials, the vanishing of the induction of a magnetization by an external magnetic field at optical frequencies is well known [3]. Nevertheless, several types of artificial nanostructures have been proposed to bypass this rule. They are generally based on the design of optically resonant building blocks (meta-atoms) of subwavelength size: the resonance warrants an efficient optical response, whereas the subwavelength size of the meta-atoms is required for a homogeneous electromagnetic response of the metamaterial or metasurface made out of them. The proposed nanostructures fall essentially into two classes, namely, plasmonic nanoclusters and high-index Mie resonators. In the first family, a set of metallic nanoobjects is organized in pairs [4] or larger clusters [5–8] to enable the excitation of loops of plasmonic currents, which generate a magnetization that oscillates at the frequency of the impinging light. In the second family, the magnetic response to light is obtained at the magnetic Mie resonances of meta-atoms of simple shapes like spheres or cylinders [9]. The resonance condition is reached when the wavelength inside the metaatom matches its size, which together with the requirement of subwavelength size imposes a high refractive material. Crystalline silicon is an excellent candidate for its large

<sup>\*</sup>Corresponding author: Mona Tréguer-Delapierre, Université de Bordeaux, CNRS, ICMCB, UMR 5026, Pessac 33600, France, e-mail: treguer@icmcb-bordeaux.cnrs.fr.

Open Access. © 2018 Mona Tréguer-Delapierre et al., published by De Gruyter. © BY-NC-ND This work is licensed under the Creative Commons Attribution-NonCommercial-NoDerivatives 4.0 License.

refractive index (~4) with low losses [9]. For both families, many experimental realizations of magnetic devices were produced by powerful "top-down" techniques such as lithography [including ultraviolet (UV), electron beam, and nanoimprint lithography, laser printing, or ion etching. The materials were mostly noble metals (Au or Ag) but also transparent conducting oxide or doped semiconductors in the first family [10] and nondoped semiconductors (silicon, germanium, tellurium) in the second family [9]. The top-down approach provides unequalled spatial resolution for the surface organization of nanosized elements. Its applications to silicon devices are particularly attractive as they present low losses, they are CMOS compatible, and the frequency of the electric and magnetic resonances can be tuned independently by a proper design of the shape of the meta-atoms [11]. Although the top-down techniques are not limited to small areas or purely 2D systems [12], their implementation becomes increasingly difficult as the size and thickness of the optical devices increase. An alternative "bottom-up" approach was proposed, which combines nanochemistry for the large-scale production of magnetic meta-atoms and self-assembly for the fabrication of thick materials [13, 14] or thin films of large area [15]. The model of isotropic magnetic nanoclusters or "plasmonic raspberries" proposed by Simovski and Tretyakov [8] in particular has stimulated a lot of synthetic efforts. Nanoclusters exhibiting a strong magnetic response were indeed successfully synthesized by several authors [16–21] and a significant variation of the effective magnetic permeability was demonstrated in a self-assembled bulk magnetic materials [20]. Although being quite valuable on a fundamental point of view, these experimental works have evidenced the need to enhance the magnetic response to reach a usable optical functionality. The highest magnetic to electric ratio of the dipolar response measured on plasmonic raspberries with silver satellites is of order 0.3 [20], a record value for meta-atoms so far but still far from the ratio of 1 required for reflective Huyghens' metasurfaces [11, 22]. Variations of the real part of the relative magnetic permeability of the bulk magnetic material assembled in Ref. [20] span an interval of 0.80-1.45, whereas possible applications to super-lensing, wave-front shaping, or impedance matching require negative, near zero, or high values of the permeability [23, 24]. Once again, nanoresonators made out of crystalline silicon prove to be highly efficient [25]. Unfortunately, silicon nanospheres of well-controlled size and crystallinity are not easily available in macroscopic amounts yet. A fair number of silicon nanospheres can be prepared and crystallized by intense laser pulses [26], but for larger amounts a productive synthetic route has still to be found [27].

We focus in this paper on the improvement of the magnetic response of plasmonic nanoclusters that are accessible to the methods of nanochemistry. However, instead of improving the structural parameters of the plasmonic raspberry model based on a large number of metallic satellites randomly distributed around a dielectric core [21], we investigated an alternative model based on a determined number of metallic satellites precisely located at the center of the faces of a Platonic solid, i.e. a convex polyhedron with 4, 6, 8, 12, or 20 faces. An example with six satellites sitting on the faces of a cube is given in Ref. [5]. We chose here the so-called dodecapod structure based on the dodecahedron Platonic solid with 12 faces. The main results of the paper are (i) that gold dodecapods (AuDDPs) can be synthesized in large amount with high purity and (ii) that the magnetic to electric polarization ratio measured on these new meta-atoms is three times higher than the reference value measured on plasmonic raspberries of similar size [18].

The paper is organized as follows: the numerical simulations that guided this work are presented in Section 2. Section 3 is devoted to the synthesis of the dodecapods, which is based on the concept of "patchy particles" [28]. The optical study is presented in Section 4. Section 5 presents the numerical simulations of the synthesized objects. Section 6 concludes the paper.

# 2 Numerical simulations of plasmonic Platonic solids

Several experimental realizations [16-21] have demonstrated the efficiency of the Simovski-Tretyakov model of plasmonic raspberries [8] for the generation of a magnetic polarization in visible light. In this model, the metallic satellites are randomly distributed around the core: neither their exact number not their precise position are controlled. On the contrary, the electromagnetic coupling between the plasmonic satellites, and hence the magnitude of the current ring generating the magnetic dipole, depends critically on the position of the satellites relative to one another. One may then wonder whether a stronger magnetic mode could be reached with a finer control of the position of the satellites. This question might have remained virtual until Chomette et al. realized the synthesis of multipod plasmonic clusters based on the geometrical model of Platonic solids decorated with 4 (tetrapods), 6 (hexapods), and 12 (dodecapods) satellites [28]. We investigated numerically the scattering properties of perfect multipods to define the most efficient morphology

and provide guidance for nanochemists. The four studied morphologies are shown in Figure 1A to D.

To identify the sole influence of the morphology, the scattering properties of the four multipods (referred to as N-pods with N=4, 6, 8, and 12) were computed keeping constant the radius of the core (50 nm) and the total volume of gold, which implies that the radius of the N satellites scales as  $N^{-1/3}$ . We employed a T-Matrix code developed by Mackowski and Mishchenko [29], providing the solution to Maxwell's equations for an ensemble of nonoverlapping spheres. Following the formalism of the Mie theory describing the scattering of a single sphere [30], the elements of the scattering matrix of the N-pods were expanded in series of scattering coefficients  $a_n^{N-pod}$  and  $b_n^{N-pod}$ . The first-order coefficients  $a_1^{N-pod}$  and  $b_1^{N-pod}$  correspond to the electric (ED) and magnetic (MD) dipolar modes, respectively,  $a_2^{N-pod}$  and  $b_2^{N-pod}$ , to the electric (EQ) and magnetic (MQ) quadrupolar modes, respectively, and so on. Figure 2A shows the scattering efficiency of the different modes computed for a dodecapod (N=12).

The scattering results essentially from three contributions namely ED, MD, and EQ. The MQ mode is much weaker and higher-order modes (not shown in Figure 2A) are negligible. The MD and ED scattering are comparable in strength in a broad band around 720 nm. Figure 2B shows the sole MD contribution of the four multipods of Figure 1. The dodecapod structure yields the highest MD scattering. The MD scattering efficiency, defined as the scattering cross-section normalized by the geometrical cross-section, reaches 1.88. The dodecapod structure is therefore chosen as the most desirable for the maximization of the magnetic response.

# 3 Synthesis

Guided by the numerical simulations reported in Section 2, we implemented a synthetic method targeting the ideal dodecapod structure of Figure 1D. Isotropic 3D

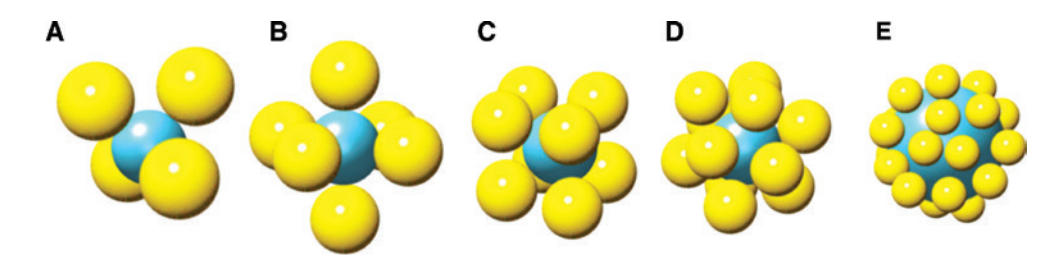


Figure 1: Illustrations of five multipode morphologies.

Sketch of the tetrapod (A), hexapod (B), octapod (C), and dodecapod (D) models used in numerical simulations with the same amount of gold distributed in N satellites around the same dielectric core (the radius of the satellites scales as  $N^{-1/3}$ ) and (E) the "plasmonic raspberry" model [8, 18].

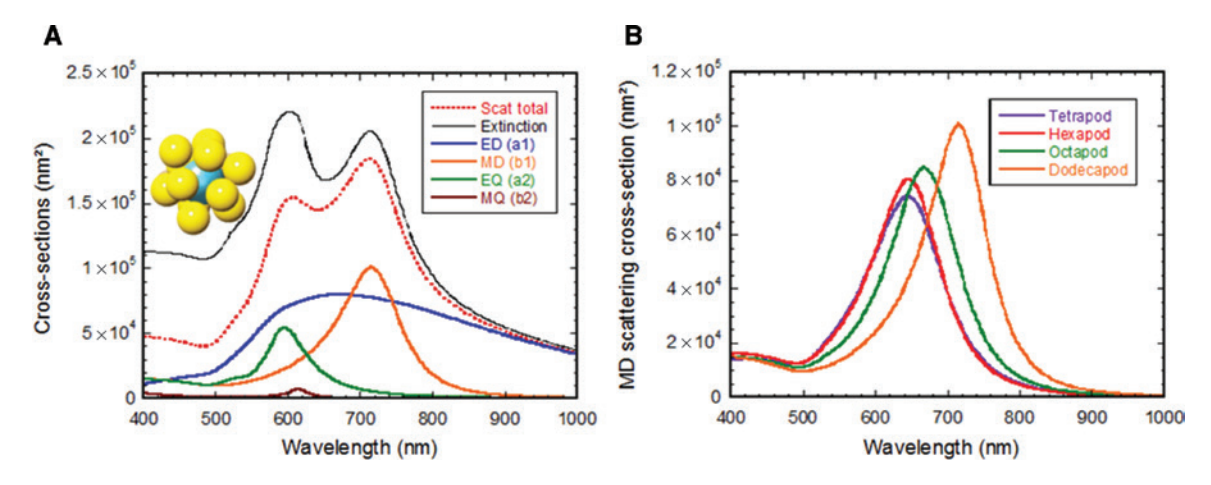


Figure 2: Simulated optical properties of the dodecapod and comparison with other multipods.

(A) Extinction and scattering cross-sections of a dodecapod in water. The radii of the silica core and gold satellites are 50 and 40 nm, respectively. The scattering is essentially dominated by the three contributions of ED, MD, and EQ. (B) MD scattering cross-section computed for the four N-pods of Figure 1A–D. The radii R(N) of the satellites are 57.7, 50.4, 45.8, and 40 nm for N = 4, 6, 8, 12, respectively, to ensure a constant volume of gold  $N.4/3\pi R(N)^3$ .

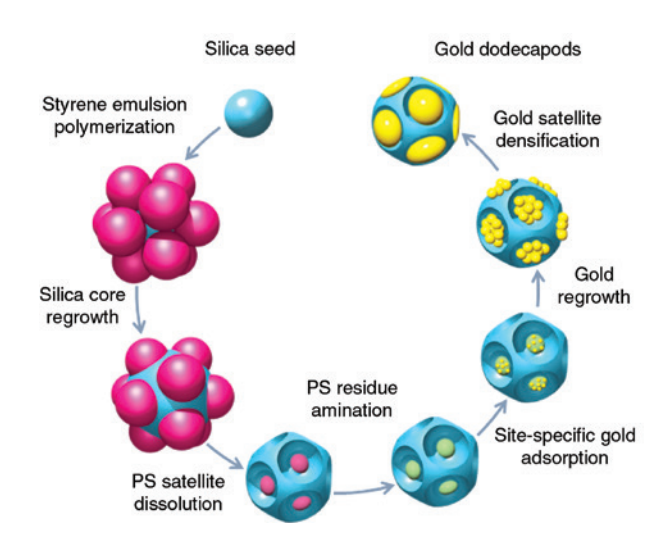


Figure 3: Schematic process for the synthesis of AuDDPs.

The growth of the polystyrene nodules defines 12 geometrical sites that are subsequently functionalized to promote gold adsorption.

The final structure is obtained after gold regrowth and thermal annealing.

plasmonic clusters were prepared by a multistep synthetic process from silica/polystyrene dodecahedral templates (Figure S1) as summarized in Figure 3. The details of the synthesis have recently been published [28]. The last three steps of the synthetic pathway shown in Figure 3 are the stages of regioselective gold seed adsorption, seed-mediated growth on the dielectric template, and condensation of the gold domains. Figure 4 shows typical dark field micrographs of the nanoobjects obtained via this approach. The electron micrographs as well as the elemental mapping evidence the well-defined patterns of the gold satellites symmetrically arranged around the silica. After the seed-mediated growth step, the 12 gold deposits consist of agglomerates of nanoparticles (Figure 4A and B). Annealing at 220°C for a couple of minutes in a polyol transforms the agglomerates into smooth, dense particles (Figure 4C and D). The size of gold particles can be adjusted by increasing the amount of gold precursor during the seed-mediated growth stage. A strong advantage of this approach is that the monodisperse golden dodecapods are produced, in high yield, at the gram scale.

Three dodecapod samples named S1–S3 with increasing amount of gold were synthesized (cf. Supporting information section for experimental details). Optical studies were performed before and after condensation of the satellites by thermal annealing. Figure S4 shows extinction measurements performed on the two sets of four samples. Suffixes NC and C stand for noncondensed and condensed, respectively, before and after annealing. Extinction curves show broad maxima, consistent with

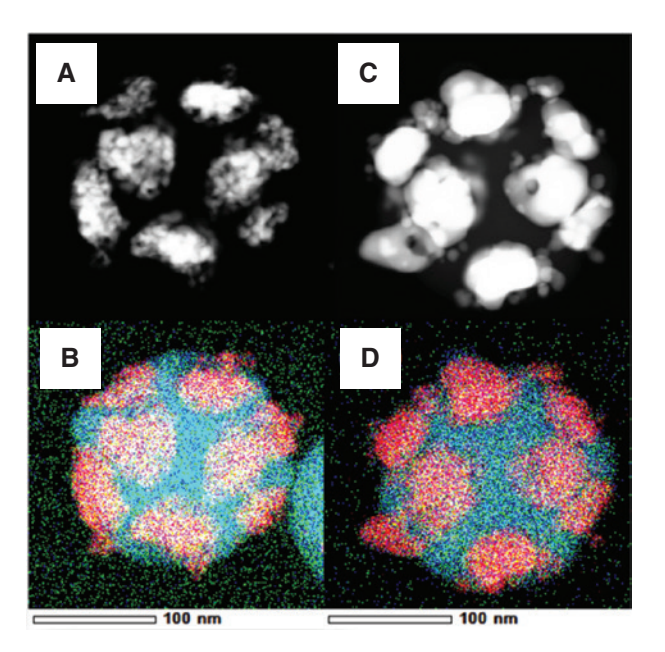


Figure 4: Synthesized dodecapods.

(A and C) SEM of dodecapods S1 before (A) and after
(C) condensation and (B and D) elemental analysis revealing silica
(blue) and gold (red). Images (A and B) and (C and D) correspond to
samples S3-NC and S3-C, respectively (see text).

plasmonic resonances. The maxima red-shift and broaden upon increasing the amount of gold.

# 4 Optical studies: static light scattering (SLS)

Following the experimental method first implemented for the study of gold raspberries [18], the scattering properties of AuDDPs were studied by polarization-resolved SLS sketched in Figure S5. The scattering angle  $\theta$  was set at 90°. The incident field  $\mathbf{E}_i$  propagating along z was linearly polarized in the (x, y) plane at angle  $\phi$  from the x axis perpendicular to the scattering plane (y, z).

We used the amplitude scattering matrix formalism for the analysis of the scattering data [30]:

$$\begin{pmatrix} E_{I/S} \\ E_{LS} \end{pmatrix} = \frac{e^{ikr}}{-ikr} \begin{pmatrix} S_2 & S_4 \\ S_3 & S_1 \end{pmatrix} \begin{pmatrix} E_i \cos \phi \\ E_i \sin \phi \end{pmatrix} \tag{1}$$

 $E_{/\!/S}$  and  $E_{\perp S}$  are the components of the scattered field parallel and perpendicular to the scattering plane. In the case of an isotropic scatterer, which we assume here, the  $S_i$  coefficients do not depend on  $\phi$  and the nondiagonal terms  $S_3$  and  $S_4$  vanish. The scattered field can be formally expanded over vector spherical harmonics of

increasing order n leading to the following expansions of  $S_1$  and  $S_2$ :

$$S_{1} = \sum_{n} \frac{2n+1}{n(n+1)} (a_{n}\pi_{n} + b_{n}\pi_{n})$$

$$S_{2} = \sum_{n} \frac{2n+1}{n(n+1)} (a_{n}\pi_{n} + b_{n}\pi_{n})$$
(2)

a and b reduce to the standard Mie scattering coefficients for spheres. For dodecapods, they are computed via the T-Matrix expansion described in Section 3. The angle-dependent coefficients  $\pi_{\perp}$  and  $\tau_{\perp}$  constructed from the Legendre polynomials are alternately odd and even functions of  $\cos\theta$  so that, for  $\theta = 90^{\circ}$ , each scattering coefficient  $a_{1}$  and  $b_{2}$  appears in either  $S_{1}$  or  $S_{2}$  but never in both. As shown in Section 3, the scattering amplitude  $S_1$  reduces to the radiation of the electric dipole ED  $(a_1)$ only, whereas  $S_2$  cumulates the radiations of the magnetic dipole MD  $(b_1)$  and the electric quadrupole EQ  $(a_2)$ [18, 20, 31].

The intensities measured along the two output polarizations for isotropic scatterers then read:

$$I_{\perp S} = I_0(\lambda) N_{DDP} \frac{\left| S_1(\theta = 90^\circ) \right|^2}{k^2} \delta \Omega g(\lambda, \delta \Omega) \cos^2 \phi = A_{\perp}(\lambda) \cos^2 \phi$$
(3a)

$$I_{I/S} = I_0(\lambda) N_{DDP} \frac{\left|S_2(\theta = 90^\circ)\right|^2}{k^2} \delta \Omega g(\lambda, \delta \Omega) \sin^2 \phi = A_{I/}(\lambda) \sin^2 \phi$$
(3b)

in which  $I_0(\lambda)$  is the spectral irradiance of the incident beam,  $N_{\rm DDP}$  is the number of AuDDPs in the scattering volume, and  $\delta\Omega$  is the solid angle of the detection window.  $g(\lambda, \delta\Omega)$  is an unknown function that accounts for the spectral sensitivity of the detector and optical transmission or reflection of all optical elements.

Experimentally, a supercontinuum laser white source (SuperK EXB-6 with SuperK Split UV-visible filter from NKT Photonics) was used to deliver a white light beam in the range of 400-900 nm onto a dilute aqueous suspension of dodecapods. The linear polarization of the incident light was set by a Glan-Taylor polarizer (Thorlabs GL5-A). A Fresnel Rhomb achromatic half-wave retarder (Thorlabs FR600HM) mounted on a motorized rotation stage was used to rotate the incident polarization by an angle  $\phi$ . The scattered light was collected at a fixed scattering angle  $\theta = 90^{\circ}$  for the two output polarizations perpendicular (signal  $I_{1s}$ ) and parallel ( $I_{1/s}$ ) to the scattering plane and delivered through a collimated fiber (NA = 0.25) to a mini-spectrometer (Hamamatsu model C10083CA) for spectral analysis.

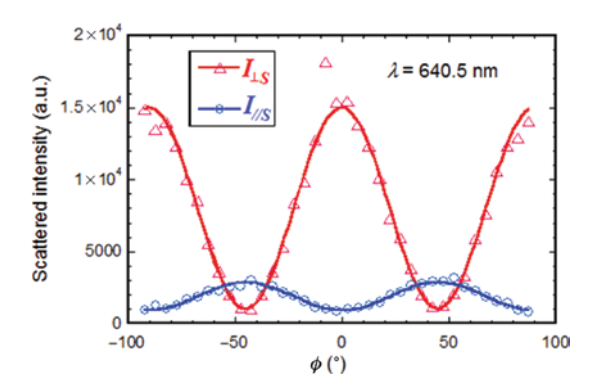


**Figure 5:** Example shown at l = 640.5 nm of the signal scattered by sample S3-C along the two output polarization channels  $I_{i,c}$  and  $I_{i,c}$ perpendicular and parallel to the scattering plane, respectively. Solid lines are a fit to  $\cos^2\phi$  and  $\sin^2\phi$  functions.

Figure 5 illustrates the data collected on sample S3-C. The perpendicular and parallel signals  $I_{\scriptscriptstyle \perp S}$  and  $I_{\scriptscriptstyle /\!/S}$  plotted at a wavelength of 640.5 nm are fitted to simple functions  $A_1\cos^2\phi + B$  and  $A_{ii}\sin^2\phi + B$ , respectively. The background signal B, identical for the two functions, does not exceed a few percent (2-7.5% across the wavelength range) of the amplitude  $A_1$ , which supports the assumption of isotropic scatterer [32].

Taking the ratio of the perpendicular to parallel signal  $A_{\mu}/A_{\mu}$  eliminates all the unknown functions in Eqs. (3a) and (3b) and provides an estimate of the strength of the magnetic dipole MD relative to ED:

$$A_{\perp}/A_{//} = \frac{\left|S_{2}(\theta = 90^{\circ})\right|^{2}}{\left|S_{1}(\theta = 90^{\circ})\right|^{2}} = \frac{\left|3b_{1} - 5a_{2}\right|^{2}}{\left|3a_{1} - 5b_{2}\right|^{2}} = \frac{MD + EQ}{ED + MQ} \approx \frac{MD}{ED}$$
(4)

This indicator of the MD/ED ratio is plotted versus wavelength for all dodecapod samples in Figure 6. It exhibits for all samples a broad maximum in the visible range. The maximum increases and red-shifts upon increasing the amount of gold from ~5% to ~9% for noncondensed dodecapods. The condensation of the satellites at a constant amount of gold further increases the maxima from ~9% to ~14%. The data measured on gold raspberries of similar size [18] are also shown in Figure 6 for comparison. Figure 6 reveals a spectacular improvement of the ratio from 4.2% for gold raspberries to 14% for dodecapods.

The parallel MD+EQ and perpendicular ED scattering cross-sections along the two polarization channels can be extracted separately by normalizing the data with a reference dispersion of calibrated silica nanoparticles ( $D_{si02}$  = 95 nm) in water [18]. The scattered

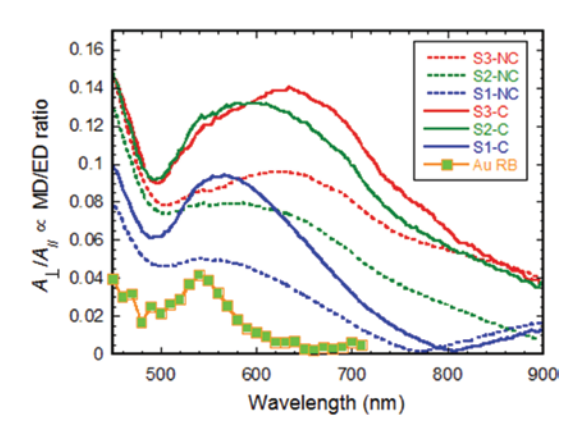


**Figure 6:** Plots of the experimental function  $A_{\perp}/A_{\parallel}$  as an estimator of the ratio of the magnetic to electric dipolar scattering. Dashed and solid lines correspond to light scattering measurements before and after condensation, respectively. The ratio increases with gold load and with condensation, well above values observed on gold raspberries shown for comparison (squares; from Ref. [18]).

intensity from the reference sample is similar to Eq. (3a) by replacing  $|S_1(\theta=90^\circ)| \, 2/k^2$  with the differential scattering cross-section  $\sigma_{ref}^{\theta=\pi/2,\;\phi=0}$  of a silica particle in water at scattering angles  $\theta=\pi/2,\;\phi=0$ , which is easily calculated from the Mie theory and scales as  $1/\lambda^4$ . The dodecapods and silica signals were collected in the same experimental conditions so that the quantities  $I_0$ ,  $d\Omega$ , and  $g(\lambda,\;d\Omega)$  are the same for dodecapods and for the reference. Dividing Eq. (3b) for dodecapods by Eq. (3a) written for the silica reference yields the differential scattering cross-sections of dodecapods along the particular directions  $\theta=\phi=90^\circ$ :

$$\sigma_{//}^{MD+EQ}(\theta = \phi = \pi/2) = \frac{\left|S_{2}(\theta = \pi/2)\right|^{2}}{k^{2}}$$

$$= K \frac{A_{//}(\lambda)}{A_{ref}^{ref}(\lambda)} \sigma_{ref}^{\theta = \pi/2, \phi = 0}(\lambda)$$
(5)

Superscript MD+EQ reminds that  $s_{//}$  is dominated by the added scattering contribution of the magnetic dipole and electric quadrupole. Figure 7A shows the plots of the parallel scattering cross-sections  $\sigma_{//}^{MD+EQ}(\theta=\phi=\pi/2)$  for three noncondensed dodecapods of increasing gold load. All three curves exhibit a clear resonance that redshifts and broadens with increasing gold amount. Due to a large uncertainty in the concentration of the dodecapods after synthesis and purification, the concentration ratio  $K=N_{re/}/N_{DDP}$  independent of wavelength could not be determined accurately for each sample. To avoid any misleading interpretation, the resonance maxima were normalized to 1. Annealing sharpens the resonances with a slight red-shift in wavelength (Figure 7B).

#### 5 Numerical simulations

The condensed dodecapods have proven to generate an MD/ED ratio about three times higher than gold raspberries of comparable size. This is a clear success of the new morphology. Nevertheless, the synthesized dodecapods are not as perfect as the ideal guiding model of Figure 1D. We refined our numerical simulations to capture the main features of the optical behavior summarized in Figures 6 and 7 and to try and understand the morphological features that cause the differences in behavior compared to

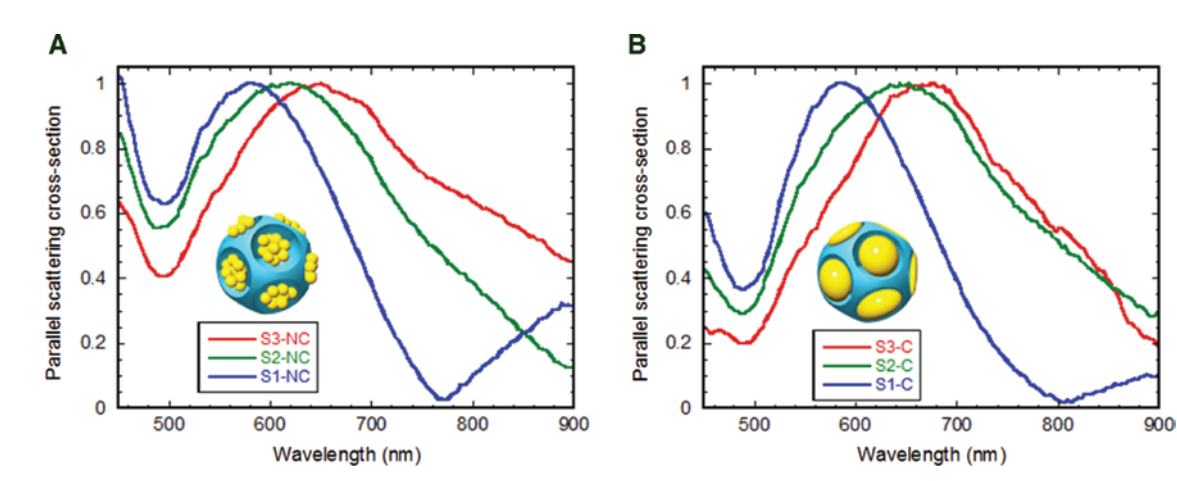


**Figure 7:** Measured parallel scattering cross-sections of uncondensed and condensed dodecapods. Parallel scattering cross-section  $\sigma_{||}^{\text{MD+EQ}}$  [Eq. (5), maximum normalized to 1] of the dodecapod samples before (A) and after (B) annealing. The resonant response red-shifts with increasing gold load. Annealing sharpens the resonance with very slight red-shift in wavelength.

the ideal case. Two different structural models were used to compute the scattering properties of the dodecapods before (noncondensed) and after (condensed) annealing.

#### 5.1 Noncondensed dodecapods

As shown in Figure 4, the satellites before annealing consist of agglomerates of gold nanoparticles. We mimic the noncondensed dodecapods as shown in Figure 8A (inset). Twelve satellite spheres of radius  $R_{\rm sat}$  were partially filled with spherical gold nanoparticles of radius  $R_{\rm hu}$  inside the volume of a truncation sphere of radius  $R_{\rm trunc}$ . Increasing the amount of gold from sample S1-NC to S3-NC may be produced by increasing  $R_{\rm trunc}$  (bigger agglomerate) and/or increasing  $R_{\rm Au}$  while keeping the number of gold nanoparticles constant (higher volume fraction of gold within each agglomerate).

Figure 8A and B shows that the experimental values of the magnetic to electric ratio  $A_{\perp}/A_{\parallel}$  (Figure 6, dashed lines) are very well reproduced by the model of aggregates of gold nanoparticles of radius 5 nm. Increasing the amount of gold in the model by increasing either the volume of the aggregate (via  $R_{\rm trunc}$ ; see Figure 8A) or the size of the gold nanoparticles ( $R_{\rm Au}$ ; see Figure 8B) enhances the magnetic response as observed experimentally. However, the experimental red-shift observed upon increasing the amount of gold is only reproduced by increasing the size of the gold nanoparticles within the aggregates, which in

turn reduces their average separation at a fixed amount of particles. This effect is consistent with the well-known plasmon ruler law stating that the resonance wavelength of a set of gold nanoparticles red-shifts as the separation of the nanoparticles is reduced [33]. This observation indicates that the size, and not just the number, of the gold grains increases upon successive regrowth steps.

#### 5.2 Condensed dodecapods

Four systems were considered, one for each volume of gold considered in the noncondensed case shown in Figure 8A. The patches are obtained by keeping the intersections of a core-sphere of radius  $R'_{\text{trunc}}$  with satellite spheres of radius  $R_{\rm sat}$ . Of course,  $R'_{\rm trunc}$  is not equal to  $R_{\rm trunc}$  as it sets to conserve the volume of gold in the system. An illustration of a typical system considered is shown in Figure 9A (inset). The scattering properties of the system are calculated using the finite element method based commercial software COMSOL Multiphysics in the scattering formalism. The field scattered by the patchy dodecapod is computed and decomposed on a spherical harmonic basis using the method of volume currents [34]. As a result, the spectral dependence of the  $a_i$  and  $b_i$  coefficients were determined, which in turn enables the calculation of the scattering coefficients  $S_1$  and  $S_2$ . Figure 9A shows how  $A_{\perp}/A_{\parallel}$  evolves as a function of wavelength. We see a clear increase in the amplitude of this magnetic to electric ratio

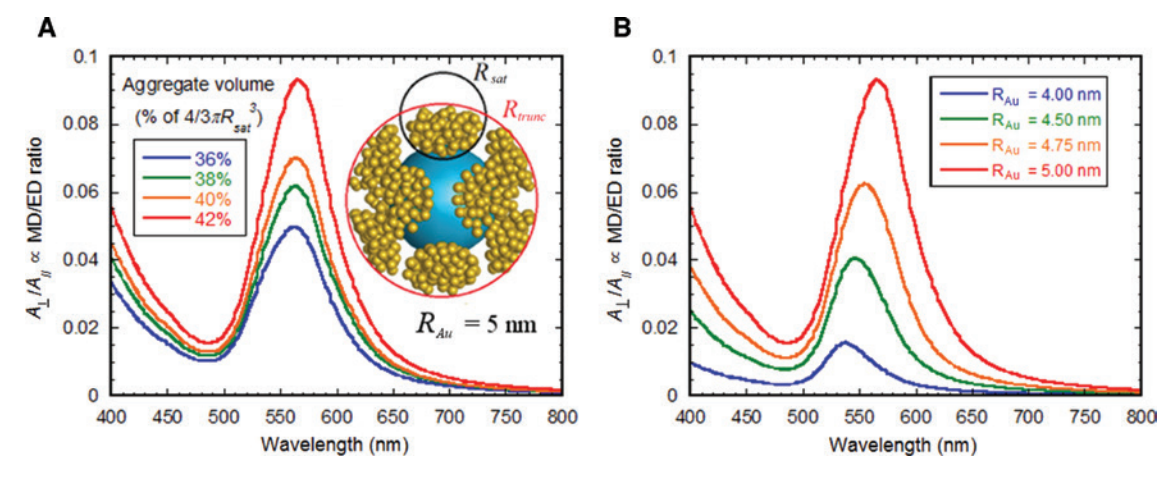


Figure 8: Simulated optical properties of uncondensed dodecapods. (A) Plot of the computed magnetic to electric estimator  $A_{\perp}/A_{\parallel}$  versus wavelength for different volumes of gold aggregates in noncondensed dodecapods. The cartoon illustrates the construction of the structure: the volume of the aggregates is defined as the intersection of 12 spherical satellites of radius  $R_{\rm sat}$  (black circle) with a truncation sphere of radius  $R_{\rm trunc}$  (red circle). These volumes are filled with nonintersecting gold nanospheres of radius  $R_{\rm Au}=5$  nm with a volume fraction set to 40%. The volume of the aggregates, controlled by  $R_{\rm trunc}$ , is given as a percentage of the volume of the full satellite sphere  $4/3\pi R_{\rm sat}^3$ . (B) Same  $A_{\perp}/A_{\parallel}$  ratio computed at constant aggregate size but for different radii  $R_{\rm Au}$ . The number of particles is kept constant; consequently, the volume fraction of gold increases. Note the red shift of the magnetic resonances with increasing size of the gold nanoparticles.

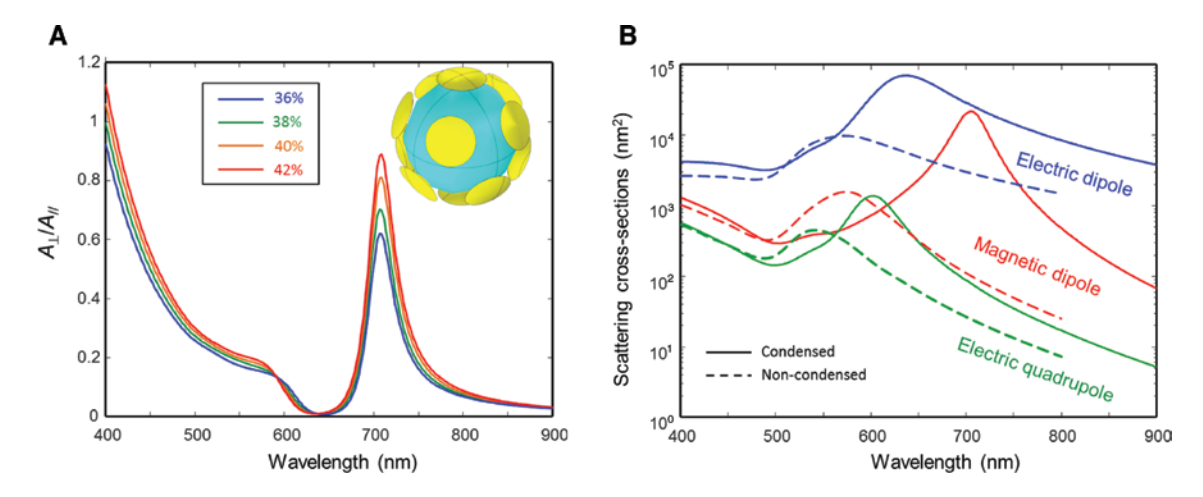


Figure 9: Simulated optical properties of condensed dodecapods. (A) Calculated plots of the computed magnetic to electric estimator  $A_{\perp}/A_{\parallel}$  versus wavelength for different volumes of gold aggregates in condensed dodecapods. The inset in the top right represents a typical model of the patchy dodecapod used in the finite element simulation. The percentages in the legend are those taken from Figure 8A and the objects have identical volumes of gold and identical values of the core particles as well as  $R_{\text{Au}}$ . (B) Simulated scattering cross-sections of the electric (blue) and magnetic dipoles (red) as well as the electric quadrupole (green) in both noncondensed (dashed line) and condensed (continuous line) cases.

as well as a red shift in the resonance wavelength compared to the noncondensed case (see Figure 8A) in accordance with the experimental observations.

The experimental behavior is qualitatively reproduced and we may discuss the reasons for which differences still remain, namely that the maximum value of  $A_{\perp}/A_{\parallel}$  (~0.10 to 0.14) is significantly lower compared to the numerical case (~1) and the red shift is not as large. The annealing process actually dewets the gold such that the shape does not necessarily conform to the same shape – intersection of two spheres resulting in a lenslike shape – as that which we simulate. This means that each patch will take on a shape that is different to the lens shape and probably more spheroidal. In the end, the simulated patches are thinner than the experimental ones resulting in larger aspect ratios that are known to resonate at higher wavelengths compared to smaller aspect ratios [35]. Furthermore, the lens shape is actually sharp along the edges, which will result in larger local fields than in the experimental case. Consequently, the capacitive effect is increased between patches, which will produce larger polarization currents and result in a larger magnetic dipole moment, hence the higher values of the magnetic to electric scattering ratio.

Getting a more refined model is certainly meaningful in the future to better guide the nanosynthesis but is beyond the scope of this paper and we find that our current understanding of the system is sufficient for a gross roadmap for improvement. In essence, the numerical system actually has great potential as its scattering properties are very good. If the nanosynthesis could be made to preserve the aspect ratio, the patchy-dodecapod system would make an excellent magneto-optical artificial magnetic resonator. As a matter of fact, as shown in Figure 9B, condensation drastically increases the amplitude of the scattering cross-sections of all multipoles present, but the most dramatic enhancement occurs from the magnetic dipole strength. This reveals the positive role of condensation of the magneto-optical properties of such systems. Furthermore, we see that the magnetic resonance of the condensed system converges toward that of the ideal dodecapod (see Figure 2A). The peak reaches a scattering cross-section of  $10^5$  nm² at a wavelength of 715 nm for the ideal case, whereas the theoretical patchy system reaches  $\sim 2 \times 10^4$  nm² at a wavelength close to 707 nm.

### 6 Conclusion

The main result of this work is the demonstration that the experimental ratio of the magnetic to electric response of AuDDPs (MD/ED=14%) is more than three times higher than its counterpart measured in gold raspberries of similar size (4.5%). This experimental result shows that the regular organization of the satellites around the core is more efficient than a random distribution for the generation of a circular current mode. This observation is fully consistent with the initial inspiring models of resonant LC inductor-capacitor nanocircuits [8, 9]. Indeed, controlling

the uniform separation of the satellites in the regular distribution warrants a constant satellite-to-satellite capacitance and therefore a sharper resonance.

As argued in Section 1, the magnetic response to light has an impact on optical functionality if its magnitude is similar to the electric response, i.e. if the ratio is about 1. AuDDPs are still below this number. It has been shown, however, that changing gold for silver reduces the optical losses and strongly enhances the MD/ED ratio of plasmonic raspberries. Up to now, the highest MD/ED ratio obtained with silver raspberries is about 0.28 [20]. Gaining a factor 3 over silver raspberries is then fully relevant to reach the target MD/ED~1. Future work will definitely have to explore the synthesis of silver dodecapods. Additional numerical results shown in Supplementary Information (Figure S5) confirm the superiority of goldsilver alloys [36]. In conclusion, we claim that the present work validates the superiority of the dodecapod structure over the disordered distribution of a larger number of smaller satellites in the raspberry model. The welldefined positions of the satellites indeed offer a better control of the collective electromagnetic coupling, which determines the strength of the circular plasmonic currents generating the magnetization.

# 7 Supplementary material

Experimental details, transmission electron microscopy (TEM) images of particles during the different stages of fabrication, and extinction spectra of the dodecahedral plasmonic particles before and after densification of the satellites.

Acknowledgments: TEM, high-resolution TEM, and highresolution scanning electron microscopy (SEM) experiments were performed at the Plateforme de Caractérisation des Matériaux of the University of Bordeaux and the Plateforme Castaing of the University of Toulouse. This work was supported by the LabEx AMADEus (ANR-10-LABX-42) and IdEx Bordeaux (ANR-10-IDEX-03-02), i.e. the Investissements d'Avenir programme of the French government managed by the Agence Nationale de la Recherche.

#### References

[1] Smith DR, Padilla WJ, Vier DC, et al. Composite medium with simultaneously negative permeability and permittivity. Phys Rev Lett 2000;84:4184-7.

- [2] Glybovski SB, Tretyakov SA, Belov PA, Kivshara YS, Simovski CR. Metasurfaces: from microwaves to visible. Phys Rep 2016;634:1-72.
- [3] Landau LD, Lifshitz EM. Electrodynamics of continuous media. Oxford, Pergamon Press, 1960.
- [4] Shalaev V. Optical negative-index metamaterials. Nat Photonics 2007;1:41-8.
- [5] Alù A, Engheta N. The quest for magnetic plasmons at optical frequencies. Opt Express 2009;17:5723-30.
- [6] Alù A, Salandrino A, Engheta N. Negative effective permeability and left-handed materials at optical frequencies. Opt Express 2006:14:1557-67.
- [7] Alù A, Engheta N. Dynamical theory of artificial optical magnetism produced by rings of plasmonic nanoparticles. Phys Rev B
- [8] Simovski CR, Tretyakov SA. Model of isotropic resonant magnetism in the visible range based on core-shell clusters. Phys Rev B 2009;79:045111.
- [9] Jahani S, Jacob Z. All-dielectric metamaterials. Nat Nanotech 2016;11:23-36.
- [10] Naik GV, Shalaev VM, Boltasseva A. Alternative plasmonic materials: beyond gold and silver. Adv Mater 2013;25: 3264-94.
- [11] Staude I, Miroshnichenko AE, Decker M, et al. Tailoring directional scattering through magnetic and electric resonances in subwavelength silicon nanodisks. ACS Nano 2013;7:7824-32.
- [12] Walia S, Shah CM, Gutruf P, et al. Flexible metasurfaces and metamaterials: a review of materials and fabrication processes at micro- and nano-scales. Appl Phys Rev 2015;2:011303.
- [13] Ponsinet V, Baron A, Pouget E, Okazaki Y, Oda R, Barois P. Self-assembled nanostructured metamaterials. EPL 2017;119:14004.
- [14] Baron A, Aradian A, Ponsinet V, Barois P. Self-assembled optical metamaterials. Opt Laser Technol 2016;82:94-100.
- Malassis L, Massé P, Treguer-Delapierre M, et al. Bottom-up fabrication and optical characterization of dense films of metaatoms made of core-shell plasmonic nanoparticles. Langmuir 2013;29:1551-61.
- [16] Mühlig S, Cunningham A, Scheeler S, et al. Self-assembled plasmonic core-shell clusters with an isotropic magnetic dipole response in the visible range. ACS Nano 2011;5:6586-96.
- [17] Sheikholeslami SN, Alaeian H, Koh AL, Dionne JA. A metafluid exhibiting strong optical magnetism. Nano Lett 2013;13: 4137-41.
- [18] Ponsinet V, Barois P, Gali SM, et al. Resonant isotropic optical magnetism of plasmonic nanoclusters in visible light. Phys Rev B 2015;92:220414(R).
- [19] Qian Z, Hastings SP, Li C, et al. Raspberry-like metamolecules exhibiting strong magnetic resonances. ACS Nano 2015;9:1263-70.
- [20] Gomez-Graña S, Le Beulze A, Treguer-Delapierre M, et al. Hierarchical self-assembly of a bulk metamaterial enables isotropic magnetic permeability at optical frequencies. Mater Horiz 2016;3:596-601.
- [21] Li C, Lee S, Qian Z, Woods C, Park S-J, Fakhraai Z. Controlling magnetic dipole resonance in raspberry-like metamolecules. J Phys Chem C 2018;122:6808-17.
- [22] Dezert R, Richetti P, Baron A. Isotropic Huygens dipoles and multipoles with colloidal particles. Phys Rev B 2017;96:180201(R).

- [23] Pendry JB. Negative refraction makes a perfect lens. Phys Rev Lett 2000;85:3966-9.
- [24] Mahmoud AM, Engheta N. Wave-matter interactions in epsilonand-mu-near-zero structures. Nat Commun 2014;5:5638.
- [25] Evlyukhin AB, Novikov SM, Zywietz U, et al. Demonstration of magnetic dipole resonances of dielectric nanospheres in the visible region. Nano Lett 2012;12:3749-55.
- [26] Zywietz U, Evlyukhin AB, Reinhardt C, Chichkov BN. Laser printing of silicon nanoparticles with resonant optical electric and magnetic responses. Nat Commun 2014;5:3402.
- [27] De Marco ML, Semlali S, Korgel BA, Barois P, Drisko GL, Aymonier C. Silicon-based dielectric metamaterials: focus on the current synthetic challenges. Angew Chem Int Ed 2018;57:2-23.
- [28] Chomette C, Tréguer-Delapierre M, Schade NB, et al. Colloidal alchemy: conversion of polystyrene nanoclusters into gold. ChemNanoMat 2017;3:160-3.
- [29] Mackowski DW, Mishchenko MI. Calculation of the T matrix and the scattering matrix for ensembles of spheres. J Opt Soc Am A 1996;13:2266-78.
- [30] Bohren CF, Huffman DR. Absorption and scattering of light by small particles. New York, Wiley-Interscience, 1983.

- [31] Sharma NL. Nondipole optical scattering from liquids and nanoparticles. Phys Rev Lett 2007;98:217402.
- [32] Gomez-Graña S, Treguer-Delapierre M, Duguet E, et al. Isotropic 3D optical magnetism in visible light in a self-assembled metamaterial. IEEE Xplore 2016.
- [33] Jain PK, Huang W, El-Sayed MA. On the universal scaling behavior of the distance decay of plasmon coupling in metal nanoparticle pairs: a plasmon ruler equation. Nano Lett 2007:7:2080-8.
- [34] Grahn P, Shevchenko A, Kaivola M. Electromagnetic multipole theory for optical nanomaterials. N J Phys 2012;14:093033-44.
- [35] Amendola V, Bakr OM, Stellacci F. A study of the surface plasmon resonance of silver nanoparticles by the discrete dipole approximation method: effect of shape, size, structure, and assembly. Plasmonics 2010;5:85-97.
- [36] Hashimoto Y, Seniutinas G, Balčytis A, et al. Au-Ag-Cu nanoalloys: tailoring of permittivity. Sci Rep 2016;6:25009-10.

Supplementary Material: The online version of this article offers supplementary material (https://doi.org/10.1515/nanoph-2018-0175).